



Aerodynamics of smart flap under ground effect

M.H. Djavareshkian ^{*,1}, A. Esmali ², A. Parsani ²

Ferdowsi University of Mashhad, Iran

ARTICLE INFO

Article history:

Received 8 June 2010

Received in revised form 5 October 2010

Accepted 20 January 2011

Available online 31 January 2011

Keywords:

Smart airfoil

Ground effect

Flap

Aerodynamic coefficients

ABSTRACT

Aerodynamic characteristics of two-dimensional smart flap under the ground effect have been assessed by a numerical simulation. In this process, a pressure-based implicit procedure to solve Navier–Stokes equations on a nonorthogonal mesh with collocated finite volume formulation is used. The boundedness criteria for this procedure are determined from the Normalized Variable Diagram (NVD) scheme. The procedure incorporates the k – ε eddy–viscosity turbulence model. Cantilever beam with uniformly varying load with roller support at the free end is considered for the configuration of the smart flap. The method is first validated against experimental data. Then, the algorithm is applied for turbulent aerodynamic flows around airfoil with smart and conventional flaps for different attack angle, flap angle and ground clearance where the results of two flaps are compared. The comparisons show that the quality of the solution is considerable.

© 2011 Elsevier Masson SAS. All rights reserved.

1. Introduction

Since the Wright brothers' first successful flight, aircraft designers have searched for ways to improve both the efficiency and performance of aircraft. Typically, aircraft wings are designed to be most efficient at a single flight condition but suffer performance penalties at other flight conditions. These penalties may be reduced through the judicious deflection of “conventional” leading- and trailing-edge hinged control surfaces. These control surfaces affect changes in the flow field by directly varying the camber in certain regions of the wing, thereby causing changes in the aerodynamic forces and moments acting on the entire wing.

Beside one of the most important considerations in airline operation is aircraft efficiency. Fuel costs can approach up to 50% of airline operating expense for some modern, wide-body, long-range transports. A 3-percent reduction of fuel consumption can produce savings of as much as \$300,000 yearly for each aircraft [19].

Due to the potential benefits of employing adaptive airfoil, there has been an intensive attempt by researchers in developing a working model. With the advancement of materials, many are now considering using smart materials to produce airfoil with variable camber capability.

New smart material technology in the aerospace industry was first introduced in 1969. More than one million of these connections have been used in military aircrafts since 1969. An analytical study conducted by NASA on the benefits of variable-camber ca-

pability reveals that drag can be significantly reduced if all wing trailing edge surfaces are available for optimization such as in the case of flight with variable camber capability [8]. In 1997, Kudva et al. [26] discussed about smart structure technologies and their benefits. Another advantage of adaptive airfoil is that it causes smaller vortex with less power [35]. Recent tests carried out on piezoelectric stimulus of adaptive airfoil, showed that they are effective to control the flutter too. It can be used a smart material to make Airplane wings or small flight devices. Gern et al. [18] succeeded in making such devices and showed that it can twist these wings more than other wings. It would increase maneuverability and improve controllability. In 2003 Forster et al. [16] designed a two-dimensional airfoil with a control surface in trailing edge that has a chord wise geometrical changes. In 2003 a joint project carried out between US aerospace research center (NASA) and Germany aerospace research center (NGC) in the field of smart wings application [15]. Another way of using smart material in airfoil is that flap ribs be made by smart material such as piezoelectric or memory alloy. In this case, a flexible structure (instead of using the joint mechanism) which features required geometric changes is made [10]. Chinnasamy and Chen [11] showed that if a smart flap is used instead of usual flap lift to drag ratio would increase. Matsuzaki and Torii [29] predicted flutter in smart wing. Gern et al. [17] show that an active control of a piezoelectric piece can delay the flutter phenomenon. Smart material could be used as wing skins. These wings are called flexible wings [28]. Abdullah and Watkins [1] succeeded in making adaptive airfoils. These airfoils can enable flight, with high lift to drag ratio throughout the flight area as well. Wickramasinghe et al. [40] made a flight device with ribs by piezoelectric fiber. The results of this structure lead to reduce the weight, the number of aileron, power and increas-

* Corresponding author.

E-mail address: javareskian@ferdowsi.um.ac.ir (M.H. Djavareshkian).

¹ Associate Professor.

² MSc student.

Nomenclature

AOA	Angle of attack	K	Factor in SBIC scheme to determine a special scheme
SA	Smart flap	AOF	Angle of flap
Re	Reynolds number	CF	Conventional flap
C	Cord length	h	Ground clearances
D	Drag force	L	Lift force
WIG	Wing-in-ground effect	SMA	Shape memory alloy
E	Young's modulus	ω_0	Weight/unit length..... N/m
B	Length of the beam	\bar{I}	Area moment of inertia m ⁴
X	Horizontal Cartesian coordinate	Y	Vertical Cartesian coordinate
$\bar{\mathbf{T}}$	Stress tensor	ρ	Density
$\bar{\mathbf{q}}$	Scalar flux vector	P	Pressure
T	Time	Γ	Diffusivity coefficient
CD	Drag coefficient	CFD	Computation fluid dynamic
SA	Spalart–Allmaras model	CL	Lift coefficient
\bar{S}	Source term	RSM	Reynolds stress model
μ	Dynamic viscosity	δv	Cell volume
F	Mass flux	I	Flux
ϕ	Scalar quantity	A	Cell face area
$\hat{\phi}$	Normalized scalar quantity	$\bar{\mathbf{V}}$	Velocity vector

ing strength. Abdullah et al. [2] studied about an adaptive airfoil system using Shape Memory Alloy (SMA) actuators.

Another way for increasing aerodynamic coefficient is used effect of ground. Wing-in-ground effect (WIG) vehicles are very efficient, which helps to increase the flight range at a reduced specific fuel consumption compared with the conventional aircraft. These phenomena happen when a wing is going near the surface. As the mass flow and height under the airfoil are decreased, pressure begins to build on the lower surface of the airfoil. Air cushion is created by the high pressure that build up under the wing. Furthermore, the induced downwash velocity diminishes close to the ground and induced drag for a wing is lowered and the effective angle of attack increases. Both occurrences result in an overall increase in the L/D ratio of the airfoil [36]. The knowledge of the effects that the ground can have on airfoils dates back to the early 1920's. In recent years, there have been successful investigations on the aerodynamics of airfoil and wing. One of the more recent wind tunnel experiments was done by Ahmed and Sharma [5,4]. This study was conducted by using a fixed and moving ground plane in a wind tunnel [6].

The dynamics of vehicles that intentionally operate in the ground proximity was studied by de Divitiis [13]. The optimal, maximum range trajectory for a glider-in-ground effect and wind shear has been analyzed by Harada [20]. Cho et al. [12] developed a boundary-element method for the conceptual design of a high-speed transportation system for flying over a nonplanar ground surface.

Kawazoe et al. [23] conduct their study on dynamic characteristics of delta wing in rolling motion near ground. Water tunnel investigation of Pairs of Vortex Filaments-in-Ground Effect has been done by Kliment and Rokhsaz [25]. Investigation of unsteady varying of ground clearance has been performed by Matsuzaki et al. [30]. Zhang and Zerihan [42] tested the aerodynamic behavior of a cambered, double element, high-lift wing in ground proximate in a wind tunnel. Aerodynamic Ground Effects of a Tailless Chevron-Shaped UCAV Model were investigated by Jones et al. [21] in the wind tunnel. Ogurek and Ashworth [32] investigated various size of winglet designs for a wing both in and out of ground effect. The aerodynamic characteristics of NACA6409 in ground proximity tested by Jung et al. [22]. Zerihan and Zhang [41] performed a computational study in order to model the flow around an inverted airfoil-in-ground effect. Smith [37] and Smith et al. [38]

performed the computational analysis of airfoils in ground effect. Patrick Vu [39] studied wing tip vortices in inverted airfoils close to the ground for use in racing car. Influence of endplate on aerodynamic characteristics for low-aspect-ratio wing-in-ground effect is performed by Park and Lee [33]. Abramowski [3] presents a numerical investigation of NACA/Munk M15 airfoil in ground proximity. Moon et al. [31] simulated three-dimensional wings-in-ground effect for aero-levitation electric vehicle. Angle et al. [7] focused their research on pitch stability analysis of an airfoil in ground effect. Numerical optimal design of a wing in-ground effect craft performed by Kim et al. [24]. Park et al. [34] present optimization of airfoil under the ground effect. Effect of ground proximity on the aerodynamic performance and stability of a light unmanned aerial vehicle has been performed by Boschetti et al. [9]. The shape optimization using the multi-objective genetic algorithm and the analysis of the 3-dimensional wings in ground effect has been performed by Lee et al. [27].

In all of the above studies, the effect of a smart wing-in-ground effect has been not assessed. To improve the advantage of flight, a smart wing can be used in near ground.

The contribution of the present paper is to simulate a smart flap under ground effect. In this simulation, the effect of attack angle, flap angle, ground clearance on airfoil with the smart and conventional flaps are assessed. The effects of turbulence models on the aerodynamic coefficients have also been investigated.

2. Numerical solution setup and conditions

2.1. Simulation smart flap deflection

In this study, smart flap deflection is designed with a cantilever beam so that the beam bending equation is the same smart flap chord deflection. Beside flap shape is a triangle (see e.g. Fig. 1), so the cantilever beams with uniformly varying load are considered (see e.g. Fig. 2). The same profile was also used by Chinnasamy and Chen [11].

The mention profile is given below:

$$Y = \frac{w_0(-X^5 + 2B^2X^3 - B^4X)}{120E\bar{I}B} \quad (1)$$

Since the parametric equation only needs, Eq. (1) is substituted by Eq. (2).

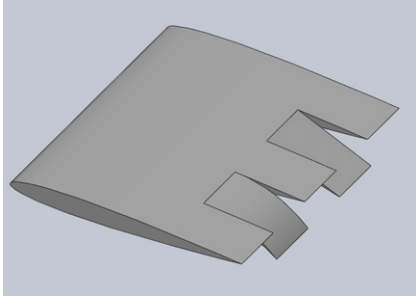


Fig. 1. Smart and convectional flaps.

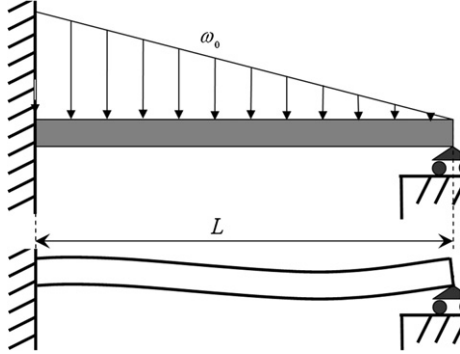


Fig. 2. Beam model.

$$\begin{aligned}
 Y_{\text{Midline}} &= k(-X^5 - aX^3 + X) \\
 Y_{\text{Upper}} &= Y_u + k_u(-X^5 - aX^3 + X) \\
 Y_{\text{Lower}} &= Y_L + k_L(-X^5 - aX^3 + X) \\
 a &= \frac{1 - B^4}{B^2} \quad (2)
 \end{aligned}$$

The bending equation can be used for midline. For upper and lower flap surfaces, the configuration was manipulated by making minor modifications. The coefficients of Eq. (2) are determined by an iterative process. Each profile is visualized using FORTRAN, and the value of the coefficient is either increased or decreased until the desired profile is obtained. A parametric smart airfoil is designed, and computational fluid dynamics simulation is done over them.

2.2. Governing equation for fluid

The basic equations, which describe conservation of mass, momentum and scalar quantities, can be expressed in the following vector form, which is independent of the used coordinate system.

$$\frac{\partial \rho}{\partial t} + \text{div}(\rho \vec{V}) = S_m \quad (3)$$

$$\frac{\partial(\rho \vec{V})}{\partial t} + \text{div}(\rho \vec{V} \otimes \vec{V} - \vec{T}) = \vec{S}_v \quad (4)$$

$$\frac{\partial(\rho \phi)}{\partial t} + \text{div}(\rho \vec{V} \phi - \vec{q}) = \vec{S}_\phi \quad (5)$$

Here ρ , \vec{V} and ϕ are density, velocity vector and scalar quantity respectively, \vec{T} is the stress tensor and \vec{q} is the scalar flux vector. The latter two are usually expressed in terms of basic dependent variables. The stress tensor for a Newtonian fluid is:

$$\vec{T} = -\left(P + \frac{2}{3}\mu \text{div} \vec{V}\right) \vec{I} + 2\mu \vec{D} \quad (6)$$

and the Fourier-type law usually gives the scalar flux vector:

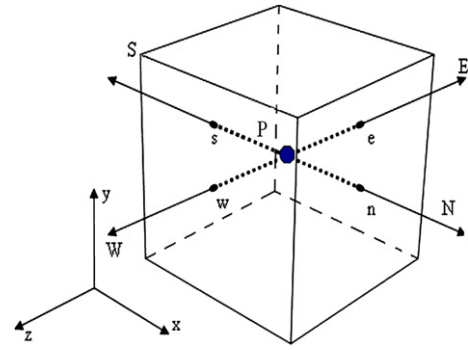


Fig. 3. Finite volume and storage arrangement.

$$\vec{q} = \Gamma_\phi \text{grad } \phi \quad (7)$$

For the purpose of illustration (5) may be expressed in 2D Cartesian coordinates as:

$$\begin{aligned}
 &\text{transient term} \quad \text{convection term} \\
 &\frac{\partial(\rho \phi)}{\partial t} + \frac{\partial(\rho u \phi)}{\partial x} + \frac{\partial(\rho v \phi)}{\partial y} \\
 &\quad \text{diffusion term} \quad \text{source} \\
 &-\frac{\partial}{\partial x} \left(\Gamma_\phi \frac{\partial \phi}{\partial x} \right) - \frac{\partial}{\partial y} \left(\Gamma_\phi \frac{\partial \phi}{\partial y} \right) = \widehat{S}_\phi \quad (8)
 \end{aligned}$$

Turbulence is accounted for by adopting the k - ε turbulence model. The governing equations for these quantities are

$$\begin{aligned}
 \frac{\partial}{\partial t}(\rho k) + \frac{\partial}{\partial x_j} \left(\rho u_j k - \Gamma_k \frac{\partial k}{\partial x_j} \right) \\
 = G - \rho \varepsilon \quad (9)
 \end{aligned}$$

$$\begin{aligned}
 \frac{\partial}{\partial t}(\rho \varepsilon) + \frac{\partial}{\partial x_j} \left(\rho u_j \varepsilon - \Gamma_\varepsilon \frac{\partial \varepsilon}{\partial x_j} \right) \\
 = C_1 \frac{\varepsilon}{k} G - C_2 \rho \frac{\varepsilon^2}{k} \quad (10)
 \end{aligned}$$

The turbulent viscosity and diffusivity coefficients are defined by

$$\mu_t = C_\mu \rho \frac{k^2}{\varepsilon} \quad (11)$$

$$\Gamma_\phi^t = \left(\frac{\mu_t}{\sigma_\phi^t} \right) \quad (12)$$

and the generation term G in Eqs. (9) and (10) is defined by

$$G = \mu_t \left[\left(\frac{\partial u_i}{\partial x_j} + \frac{\partial u_j}{\partial x_i} \right) \frac{\partial u_i}{\partial x_j} \right] \quad (13)$$

2.3. Finite-volume discretization

The discretization of the above differential equations is carried out using a finite-volume approach. First, the solution domain is divided into a finite number of discrete volumes or cells, where all variables are stored at their geometric centers (see e.g. Fig. 3). The equations are then integrated over all the control volumes by using the Gaussian theorem. The discrete expressions are presented affected with reference to only one face of the control volume, namely, e , for the sake of brevity.

For any variable ϕ (which may also stand for the velocity components), the result of the integration yields

$$\frac{\delta V}{\delta t} \left[(\rho \phi)_p^{n+1} - (\rho \phi)_p^n \right] + I_e - I_w + I_n - I_s = S_\phi \delta V \quad (14)$$

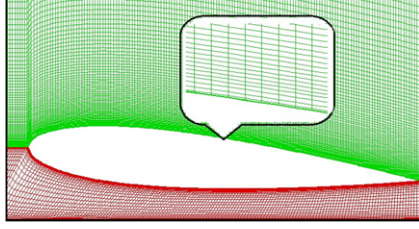


Fig. 4. Dimension of domain.

where I 's are the combined cell-face convection I^c and diffusion I^D fluxes. The diffusion flux is approximated by central differences and can be written for cell-face e of the control volume in Fig. 3 as:

$$I_e^D = D_e(\phi_p - \phi_E) - S_e^\phi \quad (15)$$

where S_e^ϕ stands for cross derivative arising from mesh nonorthogonality. The discretization of the convective flux, however, requires special attention and is the subject of the various schemes developed. A representation of the convective flux for cell-face e is:

$$I_e^c = (\rho V A)_e \phi_e = F_e \phi_e \quad (16)$$

the value of ϕ_e is not known and should be estimated by interpolation, from the values at neighboring grid points. The expression for the ϕ_e is determined by the SBIC scheme [14], that is based on the NVD technique, used for interpolation from the nodes E , P and W . The expression can be written as

$$\phi_e = \phi_W + (\phi_E - \phi_W) \tilde{\phi}_e \quad (17)$$

the functional relationship used in SBIC scheme for $\tilde{\phi}_e$ is given by:

$$\tilde{\phi}_e = \tilde{\phi}_P \quad \text{if } \tilde{\phi}_C \notin [0, 1] \quad (18)$$

where

$$\begin{aligned} \tilde{\phi}_p &= \frac{\phi_p - \phi_W}{\phi_E - \phi_W}, & \tilde{\phi}_e &= \frac{\phi_e - \phi_W}{\phi_E - \phi_W} \\ \tilde{x}_p &= \frac{x_p - x_W}{x_E - x_W}, & \tilde{x}_e &= \frac{x_e - x_W}{x_E - x_W} \end{aligned} \quad (19)$$

The limits on the selection of K could be determined in the following way. Obviously, the lower limit is $K = 0$, which would represent switching between upwind and central differencing. This is not favorable because it is essential to avoid the abrupt switching between the schemes in order to achieve the converged solution. The value of K should be kept as low as possible in order to achieve the maximum resolution of the scheme.

The final form of the discretized equation from each approximation is given as:

$$A_P \phi_P = \sum_{m=E,W,N,S} A_m \phi_m + S'_\phi + S_{dc} \quad (20)$$

Here A 's are the convection–diffusion coefficients. The term S'_ϕ in Eq. (20) contains quantities arising from nonorthogonality, numerical dissipation terms and external sources, and $(\rho \delta v / \delta t) \phi_P$ of the old time-step/iteration level (for time-dependent equation). For the momentum equations, it is easy to separate out the pressure-gradient source from the convected momentum fluxes. S_{dc} is the contribution due to the adapted deferred correction procedure.

The results are presented and discussed in the next section. At the first, grid setup and computational domain have been described.

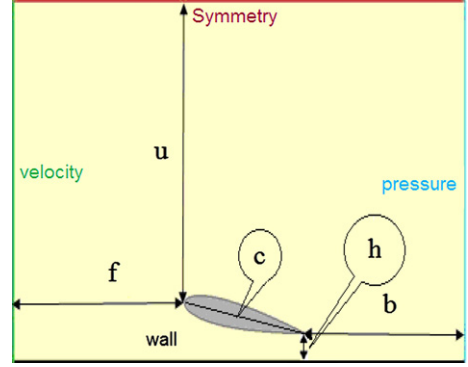


Fig. 5. Grid topology and H grid.

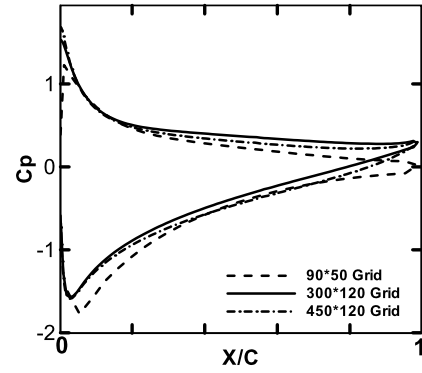


Fig. 6. Effect of grid sizing on pressure distribution on the surface of the airfoil for $AOA = 10^\circ$ and $h/c = 0.2$.

2.3.1. Grid strategy

The grid structure that used in CFD simulation was created by a structured mesh employed because of its simplicity and applicability to the current flow configuration (i.e., with a nearby ground). Schematic shape of these two-dimensional structured grids is shown in Fig. 4. According to Fig. 5 the dimension of domain has been obtained after doing several various lengths for b , f , u and independent lengths have been chosen. The grid sizing was determined after grid independence that was found by doing several different trials which show for surface pressure coefficient distribution. For example, the effect of grid size is shown in Fig. 6. For other cases, the above process is used for grid and domain independences.

2.3.2. Boundary conditions

Fig. 5 shows the boundary condition. At the inlet, velocity has been prescribed. At the outlet, the pressure is fixed. Slip boundary conditions are used on upper walls of the domain. The non-slip condition is applied at the solid walls for airfoil and ground surface. To account for the steep variations in turbulent boundary layers near solid walls, wall functions, which define the velocity profile in the vicinity of no-slip boundaries, are employed.

2.3.3. Results and discussion

The results are presented and discussed in this section. Table 1 shows the setting for numerical simulation. At the first, simulation of flow around the airfoil NACA0015 has been performed. Then, numerical investigation of flow around airfoil NACA0009 with flap in the smart and conventional conditions, the effects of angle of attack, flap angle and ground clearance have been done.

The simulation is steady and two-dimensional. Pressure coefficient distribution, lift and drag coefficients of the airfoil have been analyzed. The Reynolds number for this study is 2.4×10^5 . This

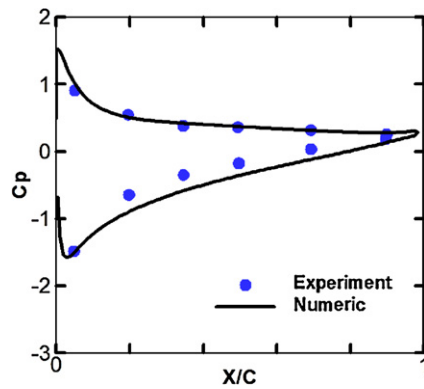


Fig. 7. Pressure coefficient distribution on the surface of the airfoil NACA 0015 for $AOA = 10^\circ$ and $h/c = 0.05$.

Table 1
Settings for numerical simulation.

Flow	Turbulent
Precision	2-D double precision
Scheme	Normalize variable diagram
Solver	SIMPLE
Turbulent model	$k-\epsilon$

Table 2
Comparison of lift and drag coefficients for airfoil NACA 0015 under different conditions.

(a) Lift coefficient			
	AOA (deg)	2.5	7.5
$h/c = 0.5$	Experiment	0.297	0.845
	Numeric	0.28	0.726
$h/c = 0.8$	Experiment	0.261	0.779
	Numeric	0.269	0.74
(b) Drag coefficient			
$h/c = 0.5$	Experiment	0.0115	0.0172
	Numeric	0.0133	0.0226
$h/c = 0.8$	Experiment	0.0118	0.0178
	Numeric	0.0133	0.0182

number indicates that the airflow has both laminar and turbulent regions.

The numerical and experimental pressure coefficients distribution on the surface of the airfoil for angles of attack 10° and ground clearance $h/c = 0.05$ is compared in Fig. 7. It can be seen that there is good agreement between present numerical and experimental data [4]. Table 2a–b also shows lift and drag coefficients for numerical and experimental data.

In actual problem the ground is moving with respect to WIG craft but in usual experimental tests, ground is fixed. Figs. 8 and 9 represent the effect of moving and fixed ground. Comparison of figures shows that the effect of the moving ground in the small ground clearance ($h/c = 0.05$) has a little effect on simulation and in high ground clearance ($h/c = 0.8$) there is not a difference between moving and fixed ground. Altogether it is not important factor in simulation. According to the experiment condition and above discussions, the ground assumed to be fixed.

The airfoil which was selected to be used in this study is the NACA0009. Airflow treatment and effect of the flap in the smart and conventional condition in ground proximity are investigated.

Fig. 10 compares smart and conventional flaps. This figure shows the surface pressure coefficient distribution of airfoil for an angle of flap 5° and $h/c = 0.5$. The lift and drag coefficients of this case also are compared in Table 3. These comparisons show that

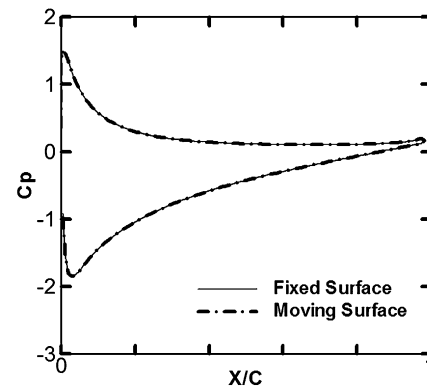


Fig. 8. Effect of fixed and moving ground on pressure distribution on the surface of the airfoil for $AOA = 10^\circ$ and $h/c = 0.8$.

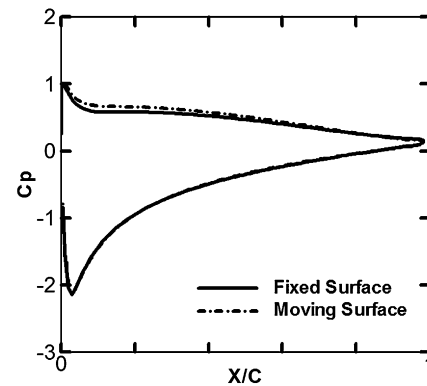


Fig. 9. Effect of fixed and moving ground on the surface of the airfoil for an angle of attack 10° and $h/c = 0.05$.

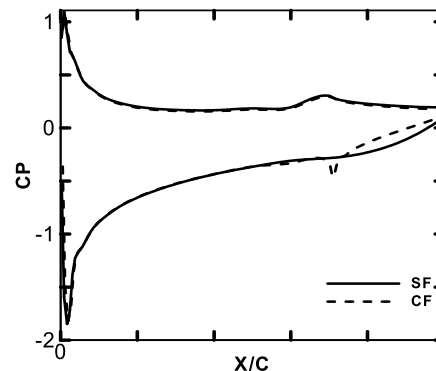


Fig. 10. Pressure coefficient distribution on the surface of the airfoil for $AOF = 5^\circ$ and $h/c = 0.5$ and $AOA = 2.5^\circ$.

the pressure coefficient distribution in the smart flap is smoothed. In the flap region, the difference between upper and lower surface pressure distribution in the smart condition is more than it in the conventional condition that lead to increase of lift. These phenomena happen because the flap and airfoil in the conventional condition are separated but in the smart condition are united. In another words, for the smart condition, airfoil and flap are single element while for conventional condition, the airfoil and flap are double element. Comparison of Table 3 data shows that the smart airfoil has larger lift and smaller drag coefficient. As result, the L/D ratio increases for the smart condition.

Figs. 11 and 12 show the effect of angle of attack on surface pressure distribution of airfoil in smart and conventional conditions respectively. An angle of flap 5° and $h/c = 0.8$ are chosen for this test. These figures show that the difference between upper

Table 3

Lift (a) and drag (b) coefficients and lift to drag ratio (c) for smart and conventional airfoils for $AOF = 5^\circ$ and $h/c = 0.5$

(a)		
AOA (deg)	Smart flap	Conventional flap
2.5	0.697	0.648
5	0.896	0.880
7.5	1.040	0.985
(b)		
2.5	0.0205	0.0210
5	0.0360	0.0363
7.5	0.0636	0.0681
(c)		
2.5	35.6	30.9
5	24.9	24.2
7.5	16.4	14.5

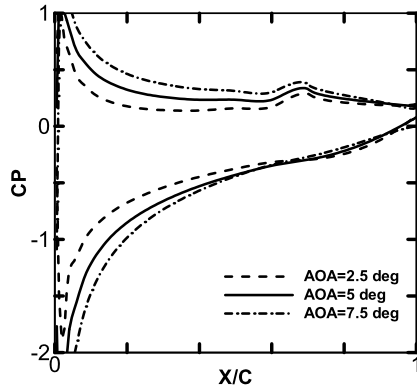


Fig. 11. Pressure coefficient distribution on the surface of the smart airfoil for $AOF = 5^\circ$ and $h/c = 0.8$.

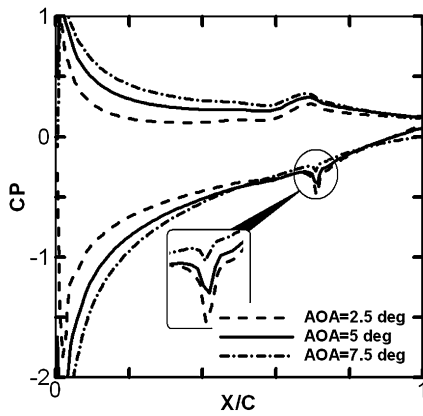


Fig. 12. Pressure coefficient distribution on the surface of the conventional airfoil for $AOF = 5^\circ$ and $h/c = 0.8$.

and lower surface pressure distribution on the entire surface of the airfoil is increased for both smart and conventional airfoils due to increase of angle of attack. These results are confirmed with the data of Table 3. As results the lift and drag coefficients increase slightly with angle of attack. Table 3c shows that the maximum L/D is in angle of flap 2.5° because at a higher angle of attack, drag increases more than lift and this condition leads to lower L/D ratio. In all of these cases the lift coefficient of the smart airfoil is higher than and the drag coefficient is lower than conventional airfoil. As a result, L/D for the smart case is higher than the conventional condition.

Figs. 13 and 14 compare the contours of the pressure coefficient around conventional airfoils for $AOF = 5^\circ$, $h/c = 0.8$ and different

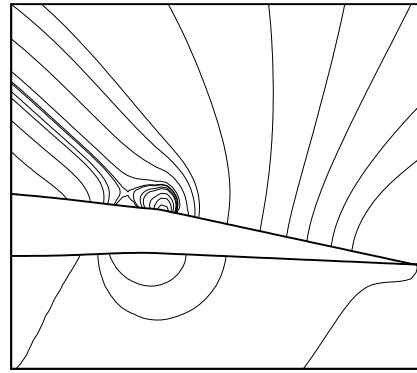


Fig. 13. Contours of pressure coefficient around the conventional airfoil for $AOF = 5^\circ$, $h/c = 0.8$ and $AOA = 2.5^\circ$.

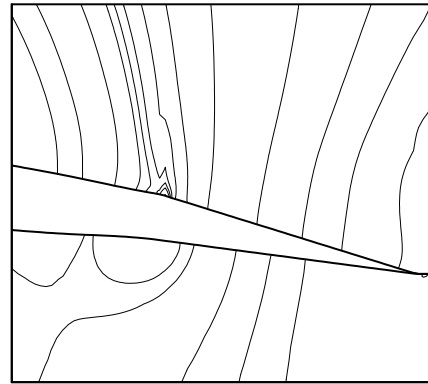


Fig. 14. Contours of pressure coefficient around the conventional airfoil for $AOF = 5^\circ$, $h/c = 0.8$ and $AOA = 7.5^\circ$.

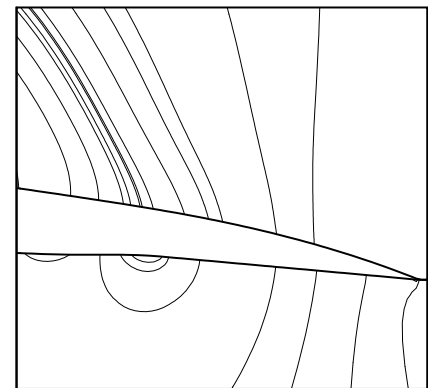


Fig. 15. Contours of pressure coefficient around the smart airfoil for $AOF = 5^\circ$, $h/c = 0.8$ and $AOA = 5^\circ$.

AOA for the conventional airfoil. It can be seen from pressure contours that the flow separation has been happened at the flap joint region for the conventional airfoil in all AOA . Comparisons show that the separation is stronger for lower AOA .

It is considerable that the discussed phenomena have not been happened in the smart airfoil and this is another advantage of the smart technology in airfoils (see e.g. Fig. 15).

Figs. 16 and 17 show the effect of angle of flap in smart and conventional conditions respectively. These figures show the surface pressure coefficient distribution of airfoil. An angle of attack 2.5° and $h/c = 0.2$ are supposed for this case. A considerable result can be seen in these cases. The figures show that the different upper and lower surface pressure distribution on the entire surface of the airfoil increase for both smart and conventional airfoils.

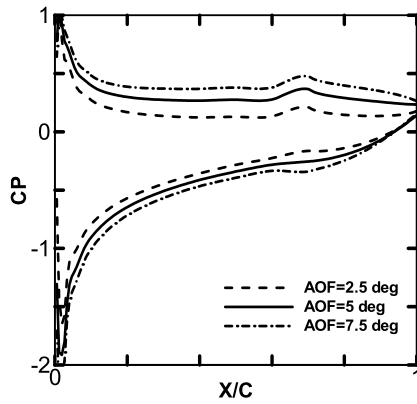


Fig. 16. Pressure coefficient distribution on the surface of the smart airfoil for AOA = 2.5° and $h/c = 0.2$.

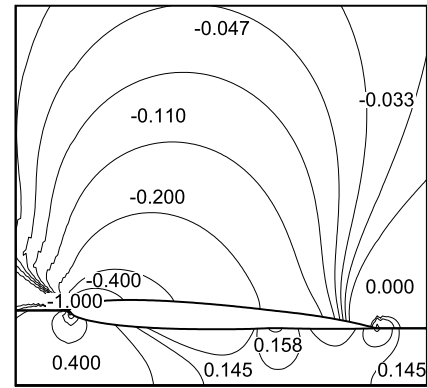


Fig. 18. Contours of pressure coefficient distribution on the surface of the smart airfoil for AOA = 2.5°, $h/c = 0.2$ and AOF = 2.5°.

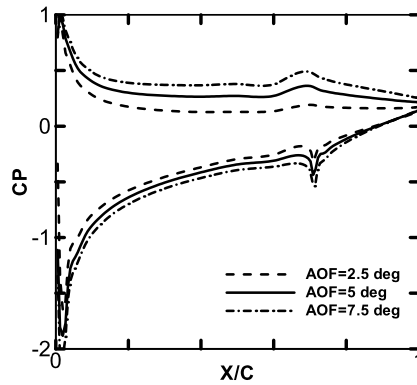


Fig. 17. Pressure coefficient distribution on the surface of the conventional airfoil for AOA = 2.5° and $h/c = 0.2$.

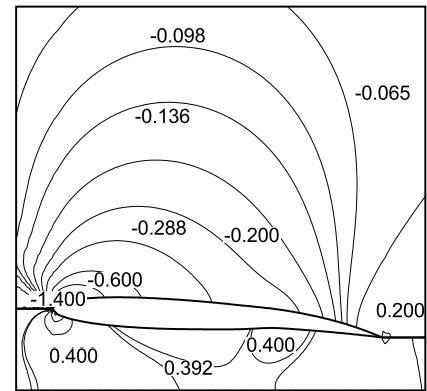


Fig. 19. Contours of pressure coefficient distribution on the surface of the smart airfoil for AOA = 2.5°, $h/c = 0.2$ and AOF = 7.5°.

Table 4
Lift (a) and drag (b) coefficients and lift-drag ratio (c) for smart and conventional airfoils for AOA = 2.5° and $h/c = 0.8$.

(a)		
AOA (deg)	Smart flap	Convectional flap
2.5	0.483	0.480
5	0.690	0.648
7.5	0.858	0.803
(b)		
2.5	0.0163	0.0170
5	0.0205	0.0210
7.5	0.0245	0.0260
(c)		
2.5	29.6	28.2
5	33.6	30.9
7.5	35.0	30.9

Table 5
Lift, drag coefficients and lift-drag ratio for smart airfoils for AOA = 2.5° and $h/c = 0.2$.

AOF (deg)	CL	CD	CL/CD
2.5	0.56	0.0103	54.369
7.5	0.932	0.018	51.778

These results show that as increasing the flap angle, the lift increases and drag decreases in each case, but the smart case has more aerodynamic performance than the conventional airfoil. Lift and drag coefficients and L/D ratio have been shown in Table 4.

Figs. 18 and 19 show the contour of pressure coefficient for AOA = 2.5°, $h/c = 0.2$ and two smart flap angles 2.5° and 7.5° respectively. The aerodynamic coefficients for these cases have been presented in Table 5. Lift and drag coefficients for AOF = 7.5° are more than AOF = 2.5°. However lift-drag coefficient ratio for AOF = 2.5° is more than AOF = 7.5°. When the angle of flap increases the pressure is higher than on the lower surface of airfoil due to 'ram pressure'. Indeed when the angle of flap increases, the passage of flow between airfoil and ground becomes narrow, flow

is blocked and so not allowing the flow stream under the wing to expand. This phenomenon also increases the flow velocity on the upper surface of the airfoil.

Fig. 20 shows surface pressure coefficient distribution of airfoil in the smart condition for AOA = 5°, angle of it flap 2.5° and different ground clearance. As can be seen in Table 6 the lift coefficient

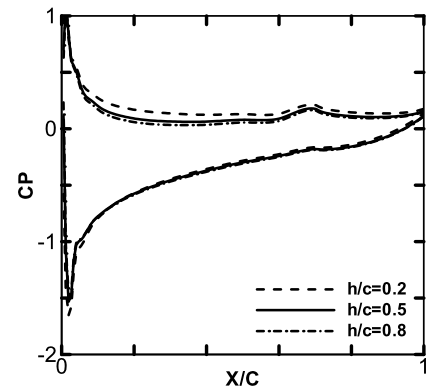


Fig. 20. Pressure coefficient distribution on the surface of the smart airfoil for AOA = 2.5° and AOF = 2.5°.

Table 6

Lift (a) and drag (b) coefficients and lift–drag ratio (c) for smart and conventional airfoils for $AOA = 5^\circ$ and $AOF = 2.5^\circ$.

(a)		
h/c	Smart flap	Convectional flap
0.2	0.802	0.801
0.5	0.735	0.728
0.8	0.718	0.707
(b)		
0.2	0.0264	0.0284
0.5	0.0279	0.0311
0.8	0.0280	0.0316
(c)		
0.2	30.4	28.2
0.5	26.3	23.4
0.8	25.6	22.3

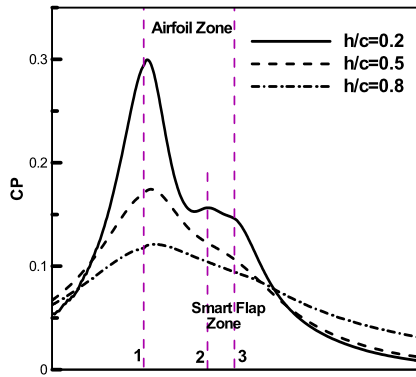


Fig. 21. Pressure coefficient distribution on the ground surface with a smart airfoil for $AOA = 2.5^\circ$ and $AOF = 2.5^\circ$.

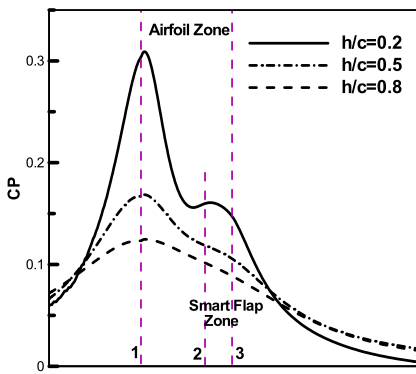


Fig. 22. Pressure coefficient distribution on the ground surface with a conventional airfoil for $AOA = 2.5^\circ$ and $AOF = 2.5^\circ$.

of the smart airfoil is larger and drag coefficient is lower than it in the conventional condition too. As results, the L/D ratio and aerodynamic performance of the smart airfoil is better than it in the conventional airfoil.

This comparison shows that for the smaller ground clearance, the pressure is higher on the lower surface of airfoil due to ‘ram pressure’. In Figs. 21 and 22, these phenomena can be seen with the pressure coefficient distribution on the ground surface. These distributions show that pressure is increased with reduction of ground clearances in both smart and conventional airfoils. Therefore, the lift coefficient increases with reduction of ground clearance. In last two figures, the pressure coefficient distributions show that maximum pressure is near the leading edge of airfoil (stagnation point) and the pressure coefficient decrease for $h/c = 0.5$ and

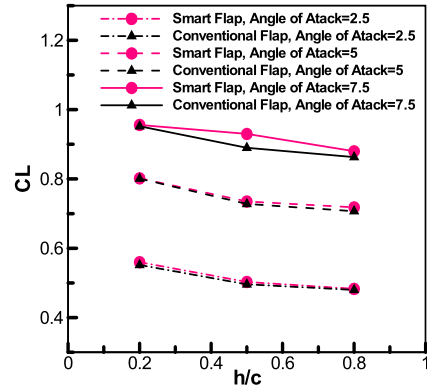


Fig. 23. Variations in CL as a function of h/c for $AOF = 2.5^\circ$.

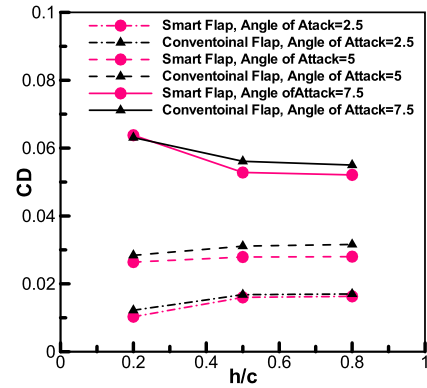


Fig. 24. Variations in CD as a function of h/c for $AOF = 2.5^\circ$.

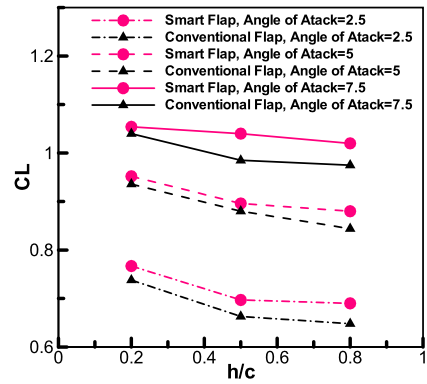


Fig. 25. Variations in CL as a function of h/c for $AOF = 5^\circ$.

0.8. But for $h/c = 0.2$, at first, the pressure coefficient decreases then increases because of converge–diverge shape of flow passage between lower surface of airfoil and the ground surface. The dash lines 2 and 3 show that the flow passage is converged and pressure coefficient decrease for both cases.

Figs. 23, 25 and 27 represent the lift coefficients for the smart and conventional airfoils for different angles of attack and flaps at varying ground clearances. The lift force was found to be approximately higher for the smart airfoil. Also lift is higher in lower ground clearances for both smart and conventional conditions. For the angle of attack 2.5° and angle of flap 2.5° , the variation of lift at varying ground clearances is in agreement with other results that discussed in previous part.

The results of drag for different angles of attack and ground clearances are shown in Figs. 24, 26 and 28 for both smart and conventional airfoils. It can be seen that the drag coefficient in-

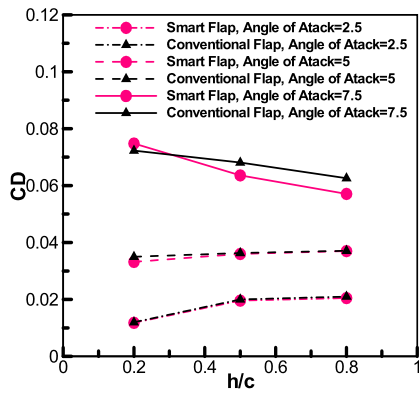


Fig. 26. Variations in C_D as a function of h/c for $AOF = 5^\circ$.

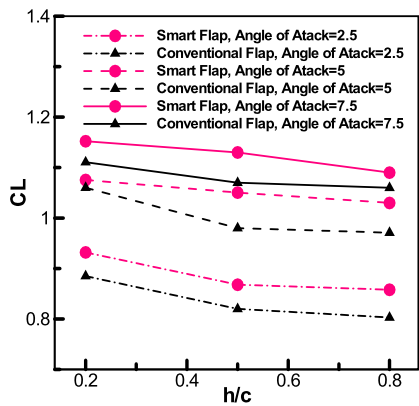


Fig. 27. Variations in C_L as a function of h/c for $AOF = 7.5^\circ$.

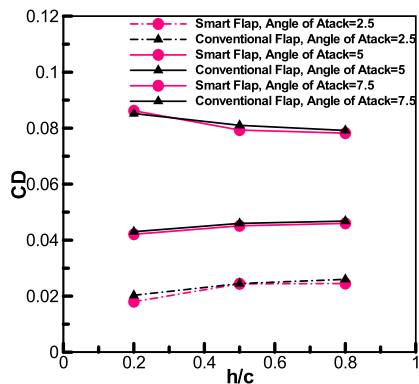


Fig. 28. Variations in C_D as a function of h/c for $AOF = 7.5^\circ$.

creasing slightly with increase ground clearance for angles of attack 2.5 and 5 but different observation was found for angles of attack 7.5 for all cases. The drag coefficient decreases slightly with ground clearance.

Several reasons for drag forces can be described. Figs. 29 and 30 describe the details of pressure distributions around the smart airfoil for an angle of flap 5° , angle of attack 2.5° , $h/c = 0.2$ and 0.8 respectively. Also contours of pressure coefficient around the smart airfoil for an angle of flap 5° , angle of attack 7.5° , $h/c = 0.2$ and 0.8 have been shown in Figs. 31 and 32 respectively. Comparison of Figs. 29 and 30 shows that the pressure distribution at the lower side of airfoil for $h/c = 0.2$ is higher than $h/c = 0.8$. Also it can be seen in Figs. 29, 30, 31 and 32 that the pressure increases slightly with angle of attack.

For low ground clearance and angle of attack 2.5 and 5, the pressure distributions under airfoil increase. As a result, the pres-

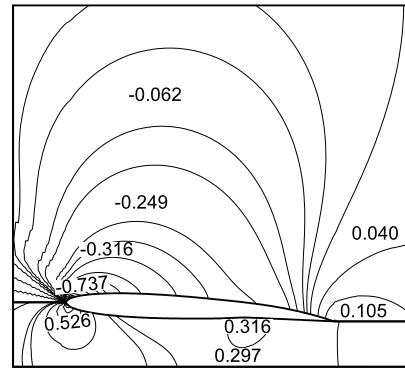


Fig. 29. Contours of pressure coefficient around the smart airfoil for $AOF = 5^\circ$, $h/c = 0.2$ and $AOA = 2.5^\circ$.

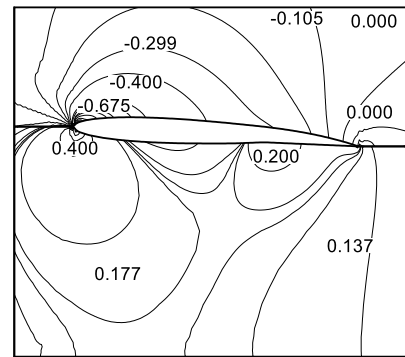


Fig. 30. Contours of pressure coefficient around the smart airfoil for $AOF = 5^\circ$, $h/c = 0.8$ and $AOA = 2.5^\circ$.

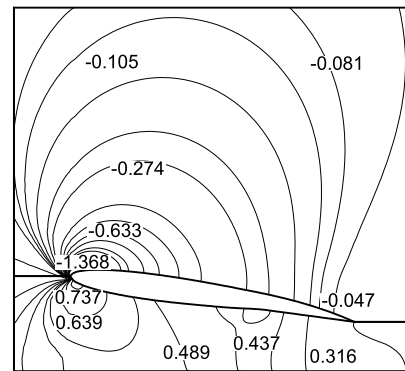


Fig. 31. Contours of pressure coefficient around the smart airfoil for $AOF = 5^\circ$, $h/c = 0.2$ and $AOA = 7.5^\circ$.

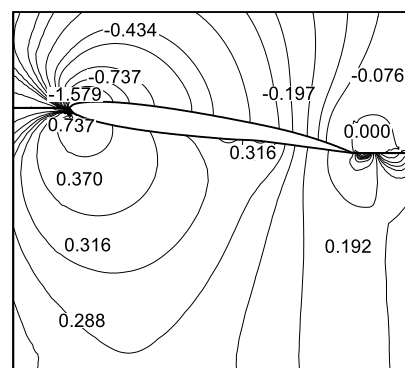


Fig. 32. Contours of pressure coefficient around the smart airfoil for $AOF = 5^\circ$, $h/c = 0.8$ and $AOA = 7.5^\circ$.

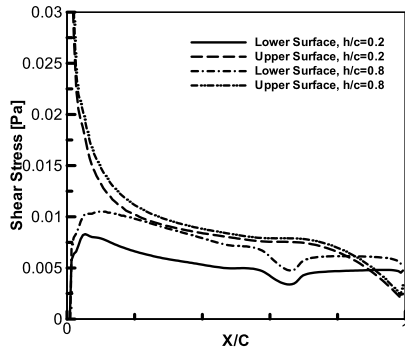


Fig. 33. Shear stress distribution on the surface of the smart airfoil for AOF = 5° and AOA = 2.5°.

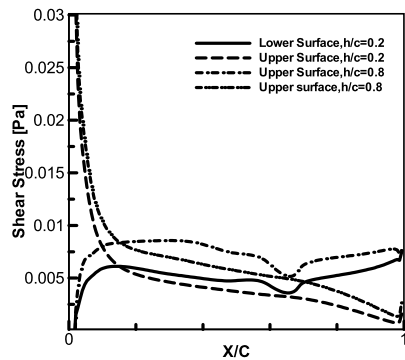


Fig. 34. Shear stress distribution on the surface of the smart airfoil for AOF = 5° and AOA = 7.5°.

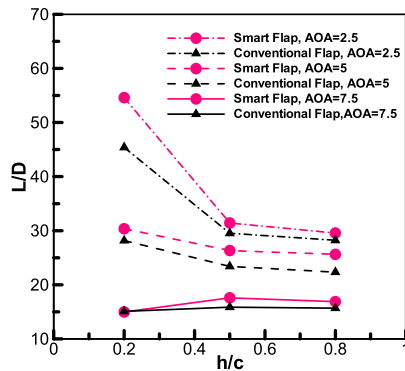


Fig. 35. Variations in L/D as a function of h/c for AOF = 2.5°.

sure drag increases. As it can be seen in Fig. 33, the surface shear stress on the upper surface for all of the ground clearance is almost equal but at the lower surface, the shear stress distribution for $h/c = 0.2$ is lower than $h/c = 0.8$. Therefore, the frictional drag is decreased for lower ground clearance.

At angle of attack 7.5°, the results show that the lower surface pressure distribution increases as the airfoil gets closer to the ground. It can also be seen in Fig. 34 that the shear stress distribution is decreased as airfoil gets closer to the ground for both upper and lower surfaces.

Table 7 shows the effect of turbulence models in simulation. Life and drag coefficients at the angle of attack 7.5°, $h/c = 0.2$ and angle of flap 5° for different turbulence models are calculated. It can be observed that drag and lift coefficients of the conventional airfoil are lower than the smart case.

Due to increase lift and decrease drag at low ground clearance, the lift–drag ratio (L/D) increases. Figs. 35–37 present the variation in L/D as a function of the ground clearance for both smart

Table 7

Lift (a) and drag (b) coefficients for AOF = 5°, $h/c = 0.2$ and AOA = 7.5°.

(a)		
Turbulence model	Smart airfoil	Conventional airfoil
SA	1.087	1.08
$k-\epsilon$ Standard	1.081	1.072
$k-\epsilon$ RNG	1.0767	1.0619
$k-\epsilon$ Realizable	1.121	1.118
$k-\omega$ Standard	1.0807	1.0744
$k-\omega$ SST	1.122	1.107
RSM	1.125	1.096
(b)		
Turbulence model	Smart airfoil	Conventional airfoil
SA	0.0914	0.0896
$k-\epsilon$ Standard	0.0876	0.0843
$k-\epsilon$ RNG	0.0755	0.0734
$k-\epsilon$ Realizable	0.0844	0.0829
$k-\omega$ Standard	0.124	0.118
$k-\omega$ SST	0.0827	0.0787
RSM	0.115	0.108

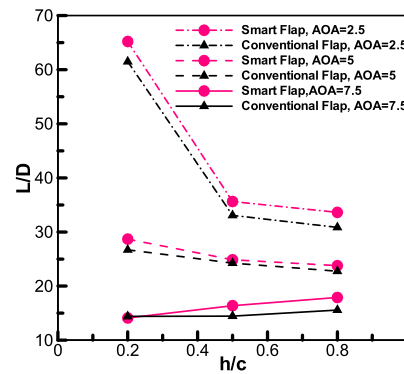


Fig. 36. Variations in L/D as a function of h/c for AOF = 5°.

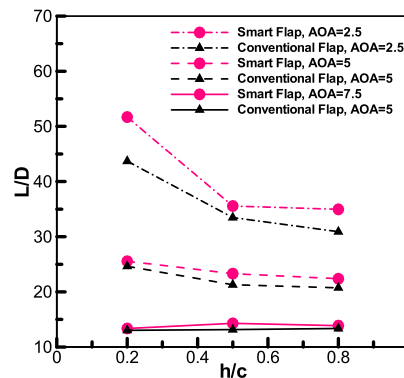


Fig. 37. Variations in L/D as a function of h/c for AOF = 7.5°.

and conventional airfoils and each angle of flap. It can be seen that the L/D is higher for the smart airfoil than the conventional case. The largest lift coefficient is for the smart airfoil at angle of flap 7.5, angle of attack 7.5 and $h/c = 0.2$. The maximum lift–drag ratio in present cases is 65 and has been happened for the smart airfoil at angle of attack 2.5, angle of flap 5 and $h/c = 0.2$. From these results, clearly that the effective lift–drag ratio depends on the operating conditions, the angle of attack, angle of flap and the ground clearance, and kind of flap and airfoil, smart and conventional.

3. Conclusion

The concept of smart wing control imposes strict requirements for the installed equipment on the wings. Traditional actuators (hydraulic, pneumatic and electrical actuators) probably do not meet

minimum requirements for such concepts. Furthermore, proposed concepts of aerodynamic control surfaces (distributed along the wing span) require fast actuation without complex mechanical systems and large energy to weight ratios. Promising solution for this purpose is the use of smart material actuator systems.

In this research, the smart flap of airfoil under the ground effect is carried out by integration of CFD. A parametric bending profile of a smart flap is designed considering different types of beams. Cantilever beam with uniformly varying load with roller support at the free end is considered here. A pressure-based implicit procedure to solve Navier–Stokes equations on a nonorthogonal mesh with collocated finite volume formulation is used to simulate. The algorithm is applied for turbulent aerodynamic flows around airfoil with smart and conventional flaps for different attack angle, flap angle and ground clearance. The main findings can be summarized as follows: 1. The agreement between presented predation and experimental data is considerable. 2. The pressure coefficient distribution in the smart flap is smoother than the conventional flap. 3. Lift–drag ratio for the smart flap is higher than the conventional flap. 4. The highest lift–drag ratio is at attack angle 2.5° . 5. The highest lift–drag ratio is at flap angle 5° . 6. The minimum ground clearance has the highest lift–drag ratio.

References

- [1] Ermira J. Abdullah, Simon Watkins, Application of smart materials for adaptive airfoil control, in: 47th AIAA Aerospace Sciences Meeting Including the New Horizons Forum and Aerospace Exposition, Orlando, Florida, 5–8 January 2009.
- [2] Ermira J. Abdullah, Bil Cees, Simon Watkins, Numerical simulation of an adaptive airfoil system using SMA actuators, in: 48th AIAA Aerospace Sciences Meeting Including the New Horizons Forum and Aerospace Exposition, 4–7 January 2010.
- [3] Tomasz Abramowski, Numerical investigation of airfoil in ground proximity, *Journal of Theoretical and Applied Science* 45 (2) (2007) 425–436.
- [4] M.R. Ahmed, S.D. Sharma, An investigation on the aerodynamics of a symmetrical airfoil in ground effect, *Experimental Thermal and Fluid Science* 29 (2005) 633–647.
- [5] M.R. Ahmed, S.D. Sharma, Experimental investigation of the flow field of a symmetrical airfoil in ground effect, in: 21st Applied Aerodynamics Conference, Orlando, Florida, 2003.
- [6] M.R. Ahmed, T. Takasaki, Y. Kohama, Experiments on the aerodynamics of a cambered airfoil in ground effect, in: 44th AIAA Aerospace Sciences Meeting and Exhibit, Reno, Nevada, 2006.
- [7] Gerald M. Angle, Brian M. O'Hara, Franz A. Pertl, James E. Smith, Pitch stability analysis of an airfoil in ground effect, *Journal of Aircraft* 46 (3) (2009).
- [8] A. Bolonkin, G.B. Gilyard, Estimated benefits of variable-geometry wing camber control for transport aircraft, NASA TM 1999-206586, 1999.
- [9] Pedro J. Boschetti, Elsa M. Cárdenas, Andrea Amerio, Stability and performance of a light unmanned airplane in ground effect, in: 48th AIAA Aerospace Sciences Meeting Including the New Horizons Forum and Aerospace Exposition, Florida, 2010.
- [10] Lucio Flavio Campanile, Stefan Anders, Aerodynamic and aeroelastic amplification in adaptive belt-rib airfoils, *Aerospace Science and Technology* 9 (2005) 55–63.
- [11] Parthasarathy Chinnasamy, Yitung Chen, Application of computational fluid dynamics on smart wing design, in: 43th AIAA Aerospace Sciences Meeting and Exhibit, Reno, Nevada, 10–13 January 2005.
- [12] Jeonghyun Cho, Jinsoo Cho, Seawook Lee, Unsteady numerical simulation of wings with flapper flying over non-planar ground surface, *Journal of Aircraft* 44 (6) (2007).
- [13] Nicola de Divitiis, Performance and stability of a winged vehicle in ground effect, *Journal of Aircraft* 42 (1) (2005).
- [14] M.H. Djavarehshkian, A new NVD scheme in pressure-based finite-volume methods, in: 14th Australasian Fluid Mechanics Conference, Adelaide University, Adelaide, Australia, 10–14 December 2001, pp. 339–342.
- [15] Jennifer P. Florance, Alpheus W. Burner, Gary A. Fleming, Craig A. Hunter, Sharon S. Graves, Contributions of the NASA Langley Research Center to the DARPA/AFRL/NASA/NORTHROP GRUMMAN Smart Wing Program, in: 44th AIAA/ASME/ASCE/AHS Structures, Structural Dynamics, and Materials Conference, Norfolk, Virginia, 7–10 April 2003.
- [16] E. Forster, B. Sanders, F. Eastep, Synthesis of a variable geometry trailing edge control surface, in: 44th AIAA/ASME/ASCE/AHS Structures, Structural Dynamics, and Materials Conference, Norfolk, Virginia, 7–10 April 2003.
- [17] Frank H. Gern, Daniel J. Inman, Rakesh K. Kapania, Structural and aeroelastic modeling of general platform wings with morphing airfoils, *AIAA Journal* 40 (4) (2002).
- [18] Frank H. Gern, Daniel J. Inman, Rakesh K. Kapania, Computation of actuation power requirements for smart wings with morphing airfoils, *AIAA Journal* 43 (12) (2005).
- [19] G.B. Gilyard, J. Georgie, J.S. Barnicki, Flight test of an adaptive configuration optimization system for transport aircraft, NASA TM 1999-206569, 1999.
- [20] Masanori Harada, Optimal trajectory of a glider in ground effect and wind shear, in: AIAA Guidance, Navigation and Control Conference and Exhibit, California, 2005.
- [21] B.L. Jones, M.E. Franke, E.J. Stephen, Aerodynamic ground effects of a tailless chevron-shaped UCAV model, in: 24th Applied Aerodynamics Conference, San Francisco, California, 2006.
- [22] K.H. Jung, H.H. Chun, H.J. Kim, Experimental investigation of wing-in-ground effect with a NACA6409 section, *Journal of Marine Science and Technology* 13 (2008) 317–327.
- [23] H. Kawazoe, T. Yorikane, Y. Tone, A study on dynamic characteristics of delta wing in rolling motion near ground, in: 39th AIAA Aerospace Sciences Meeting & Exhibit, Reno, NV, 2001.
- [24] Hee Jung Kim, Ho Hwan Chun, Kwang Hyo Jung, Aeronumeric optimal design of a wing-in-ground-effect craft, *Journal of Marine Science and Technology* (2009), doi:10.1007/s00773-008-0020-7.
- [25] Linda K. Kliment, Kamran Rokhsaz, Experimental investigation of pairs of vortex filaments in ground effect, in: 36th AIAA Fluid Dynamics Conference and Exhibit, San Francisco, California, 2006.
- [26] Jayanth N. Kudva, Kari Appa, Christopher A. Martin, A. Peter Jardine, Design, Fabrication and Testing of the DARPA Wright Lab Smart Wing Wind Tunnel Model, American Institute of Aeronautics and Astronautics (AIAA), 1997.
- [27] Juhee Lee, Chol-Ho Hong, Byeong Sam Kim, Kyoungwoo Park, Kwan Ahn Jong, Optimization of wings in ground effect using multi-objective genetic algorithm, in: 48th AIAA Aerospace Sciences Meeting Including the New Horizons Forum and Aerospace Exposition, Florida, 2010.
- [28] Manoranjan Majji, Othon K. Rediniotis, John L. Junkins, Design of a morphing wing: modeling and experiments, in: AIAA Atmospheric Flight Mechanics Conference and Exhibit, Hilton Head, South Carolina, 20–23 August 2007.
- [29] Yuji Matsuzaki, Hiroshi Torii, Flutter boundary prediction of an adaptive smart wing during process of adaptation using steady-state response data, in: 47th AIAA/ASME/ASCE/AHS Structures, Structural Dynamics, and Materials Conference, Newport, Rhode Island, 1–4 May 2006.
- [30] Takahisa Matsuzaki, Kato Takuma, Yoshioka Shuya, Kohama Yasuaki, Study of unsteady characteristics of wings in ground effect, in: Third International Symposium on Trans Disciplinary Fluid Integration, Matsushima, Miyagi, Japan, 2006.
- [31] Young J. Moon, Hyeon-Joon Oh, Jung-Hee Seo, Aerodynamic investigation of three-dimensional wings in ground effect for aero-levitation electric vehicle, *Aerospace Science and Technology* 9 (2005) 485–494.
- [32] David J. Ogurek, Jeff Ashworth, Experimental investigation of various winglet designs for a wing in ground effect, in: 22nd Applied Aerodynamics Conference and Exhibit, Providence, Rhode Island, 2004.
- [33] Kyoungwoo Park, Juhee Lee, Influence of endplate on aerodynamic characteristics of low-aspect-ratio wing in ground effect, *Journal of Mechanical Science and Technology* 22 (2008) 2578–2589.
- [34] Kyoungwoo Park, Byeong Sam Kim, Juhee Lee, Kwang Soo Kim, Aerodynamics and optimization of airfoil under ground effect, in: Proceedings of World Academy of Science, Engineering and Technology, vol. 40, ISSN: 2070-3740, 2009.
- [35] Nan Jou Pern, J.D. Jacob, Wake Vortex Mitigation Using Adaptive Airfoils, American Institute of Aeronautics and Astronautics (AIAA), 1999.
- [36] K.V. Rozhddestvensky, Aerodynamics of a Lifting System in Extreme Ground Effect, Springer, Berlin, 2000, p. 1.
- [37] Justin L. Smith, Computational analysis of airfoils in ground effect for use as a design tool, MSc thesis, Mechanical and Aerospace Engineering Department, Morgantown, West Virginia, 2007.
- [38] Justin L. Smith, Henry Z. Graham, James E. Smith, The validation of an airfoil in the ground effect regime using 2-D CFD analysis, in: 26th AIAA Aerodynamic Measurement Technology and Ground Testing Conference, Seattle, Washington, 2008.
- [39] Patrick Vu, CFD study of wing tip vortices for inverted airfoils in ground effect, MS thesis, School of Engineering, Cranfield University, 2006.
- [40] Viresh K. Wickramasinghe, Yong Chen, Marcias Martinez, Robert Kernagha, Franklin Wong, Design and verification of smart wing for an extremely-agile micro-air-vehicle, in: 50th AIAA/ASME/ASCE/AHS/ASC Structural Dynamics, and Materials Conference, Palm Springs, California, 4–7 May 2009.
- [41] Jonathan Zerihan, Xin Zhang, Aerodynamics of a single element wing in ground effect, in: 38th AIAA Aerospace Sciences Meeting and Exhibit, Reno, Nevada, January 2000.
- [42] Xin Zhang, Jonathan Zerihan, Aerodynamics of a double element wing in ground effect, in: 40th AIAA Aerospace Sciences Meeting and Exhibit, Reno, Nevada, 2002.